Journal of the European Ceramic Society 39 (2019) 3703–3709

Contents lists available at ScienceDirect

Journal of the European Ceramic Society

journal homepage: www.elsevier.com/locate/jeurceramsoc

Original Article

Excellent energy-storage properties of $NaNbO_3$-based lead-free antiferroelectric orthorhombic P-phase (Pbma) ceramics with repeatable double polarization-field loops

He Qi[a], Ruzhong Zuo[a,*], Aiwen Xie[a], Jian Fu[a], Dou Zhang[b]

[a] Institute of Electro Ceramics & Devices, School of Materials Science and Engineering, Hefei University of Technology, Hefei, 230009, PR China
[b] State Key Laboratory of Powder Metallurgy, Central South University, Changsha, Hunan, 410083, PR China

ARTICLE INFO

Keywords:
Lead-free antiferroelectric ceramics
Energy-storage capacitor
Field induced phase transition
Stability of antiferroelectricity

ABSTRACT

The energy-storage performance of stable $NaNbO_3$-based antiferroelectric (AFE) ceramics was for the first time reported in (0.94-*x*)$NaNbO_3$-0.06$BaZrO_3$-*x*$CaZrO_3$ lead-free ceramics. A gradual evolution from an instable AFE phase ($x \leq 0.01$) to an orthorhombic AFE P phase (*Pbma*) ($0.01 < x \leq 0.05$) was found to accompany the appearance of repeatable double-like polarization versus electric field loops although poled samples ($x < 0.01$) own an AFE monoclinic phase ($P2_1$). Interestingly, compared with $x \leq 0.01$ samples with instable antiferroelectricity, a relatively high recoverable energy storage density W_{rec} ~ 1.59 J/cm^3 (@ 0.1 Hz) and a storage efficiency η of ~30% were achieved in the $x = 0.04$ ceramic. Moreover, a high W_{rec} of > 1.16 J/cm^3 and an outstanding charge-discharge performance with fast discharge rate ($t_{0.9} < 100$ ns) were generated in the temperature range from room temperature to 180 °C in the $x = 0.04$ ceramic. These results suggest that $NaNbO_3$-based AFE P-phase ceramics could be new potential dielectric materials for high-energy storage capacitors.

1. Introduction

Increasing demand for efficient energy-storage devices has drawn considerable attention in recent years [1]. Dielectric ceramic capacitors exhibit obvious advantages in energy storage properties owing to the fast charge and discharge rate, superior mechanical and thermal properties compared with batteries, supercapacitors and polymer capacitors [2,3]. The recoverable energy-storage density W_{rec} and efficiency η of a capacitor can be determined according to a polarization-electric field (*P-E*) loop during a charge-discharge period using the following formula: $W_{rec} = \int_{P_r}^{P_{max}} EdP$, $W_{loss} = \int PdE$, and $\eta = W_{rec}/(W_{rec} + W_{loss})$, where *Pmax* is the saturated polarization, P_r is the remanent polarization, and W_{loss} is the area of hysteresis loop [4,5]. Owing to the existence of high *Pmax* and low P_r during the process of electric field induced reversible antiferroelectric (AFE)-ferroelectric (FE) phase transition, AFE perovskites show obvious advantages compared with FE perovskites and linear dielectric materials [4–9]. Various types of AFE ceramics have been so far investigated as an effort to improve their energy-storage density, especially for lead-free ceramics in recent years due to the pollution of lead oxides [10–14].

$NaNbO_3$ (NN) [14–17], $(Bi_{1/2}Na_{1/2})TiO_3$ (BNT) [12,13,18] and $AgNbO_3$ (AN) [10,11,19] are the most widely studied lead-free AFE materials up to now. Excellent energy storage properties have been achieved in both BNT and AN-based lead-free AFE solid solutions [10–13]. Comparatively speaking, the energy storage density of NN-based AFE ceramics is inferior [14]. Similar to AN, NN is a well-documented AFE perovskite compound and exhibits an AFE orthorhombic (AFE_O) *Pbma* space group (P phase) at room temperature (RT) and a number of other phases with the deviation of temperature from RT [20]. However, the AFE_O P phase in pure NN ceramics was found to irreversibly change into FE orthorhombic Q phase with $P2_1ma$ space group at RT under an external field owing to their similar free energies between coexisting AFE phases and FE Q phases [21,22]. As a result, the antiferroelectricity of pure NN cannot be repeatedly used. Therefore, to effectively take advantage of the antiferroelectricity of NN for the application of energy-storage capacitors, one critical issue to be solved is how to adequately enhance the antiferroelectric stability. A couple of studies have been carried out on attempting to stabilize the antiferroelectricity of NN and to achieve repeatable field induced AFE-FE phase transition from the crystallographic point of view [23–25], more focusing on the electrical field induced strain performances. A recent study reported an energy-storage density of W_{rec}~0.55 J/cm^3 at RT in AFE and FE phase coexisted NN-$CaZrO_3$ (NN-CZ) solid solutions [14], where such a low W_{rec} value was partially ascribed to the fact that

* Corresponding author.
E-mail address: piezolab@hfut.edu.cn (R. Zuo).

https://doi.org/10.1016/j.jeurceramsoc.2019.05.043
Received 19 February 2019; Received in revised form 21 May 2019; Accepted 24 May 2019
Available online 26 May 2019

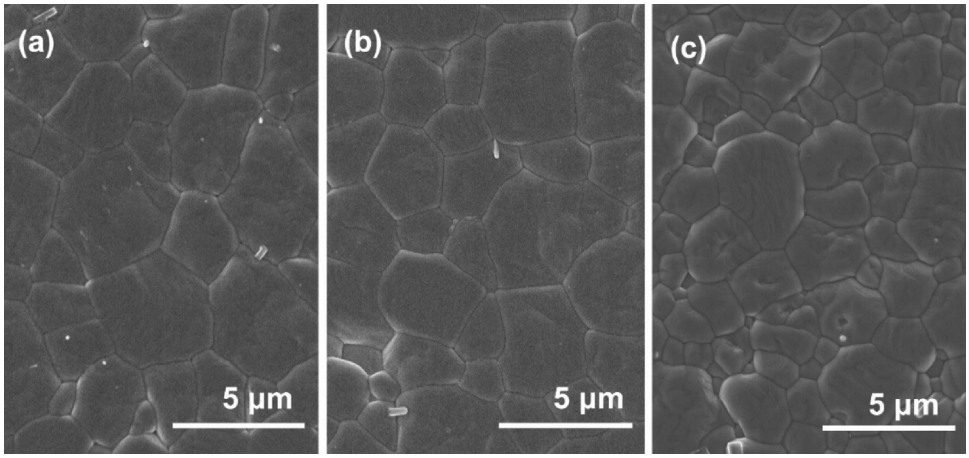

Fig. 1. SEM micrographs on polished and thermally etched surfaces of (0.94-*x*)NN-0.06BZ-*x*CZ ceramics sintered at their optimum temperatures: (a) $x = 0$, (b) $x = 0.02$ and (c) $x = 0.04$.

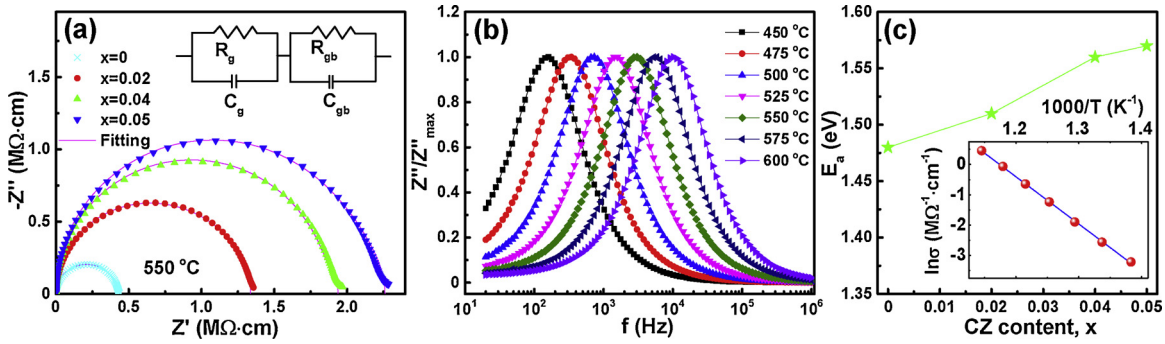

Fig. 2. (a) The complex AC impedance and fitting semicircles at 550 °C for the (0.94-*x*)NN-0.06BZ-*x*CZ ceramics; (b) plots of *Z''/Z''max* versus frequency in the temperature range 450–600 °C for the $x = 0.04$ ceramic; and (c) the variation of the E_a with CZ content. The inset of (c) is the Arrhenius-type plots of bulk conductivity for the $x = 0.04$ ceramic.

the breakdown strength (E_B) was much lower than the driving field of the AFE-FE phase transition.

As far as the literature survey is concerned, the energy-storage density of stable NN-based AFE solid solution ceramics has not yet been reported so far. A reproducible double *P-E* hysteresis loop has clearly revealed a stable antiferroelectricity at RT in NN-$BaZrO_3$-CZ (NN-BZ-CZ) solid solutions in Ref. [25] with much attention to the correlation between the phase stability and the field induced strain. In this work, a special focus was placed on the energy-storage properties of the NN-BZ-CZ ternary system. The composition, temperature and frequency dependence of W and η values were explored in detail. Moreover, the energy-storage performance of only post-poled samples was evaluated, considering the fact that an irreversible AFE-FE phase transition should be involved if the AFE phase is not stable.

2. Experimental procedure

The (0.94-*x*)NN-0.06BZ-*x*CZ ($0 \le x \le 0.05$) ceramics were manufactured by a conventional solid-state reaction method. Commercially available reagent grade oxide and carbonate powders were used as the starting materials. The powders were mixed thoroughly in ethanol using zirconia balls for 6 h according to their compositional formula. The powder was calcined at 900 °C for 3 h and then ball-milled again for 10 h, and finally pressed into disk samples with a diameter of 10 mm under 100 MPa using polyvinyl alcohol (PVA) as a binder. Sintering was performed in the temperature range of 1350˜1380 °C for 2 h in covered alumina crucibles after burning out the binder at 550 °C for 4 h. Silver electrodes were and pasted and then fired on both sides of the samples at 550 °C for 30 min. The compositions with $0 \le x \le 0.01$ and $0.02 \le x \le 0.05$ were poled at RT under a dc field of 15 kV/mm and 20 kV/mm for 15 min, respectively.

Dielectric properties as a function of temperature and frequency were measured by an LCR meter (Agilent E4980A, Santa Clara, CA, USA). The domain morphology was observed on a field-emission transmission electron microscope (FE-TEM, JEM-2100 F, JEOL, Japan) operated at 200 kV. The surface morphology of the samples was observed using a field-emission scanning electron microscope (FE-SEM; SU8020, JEOL, Tokyo, Japan). Before the SEM observation, the disk samples were polished and then thermally etched at a temperature of ˜150 °C lower than the sintering temperature for 30 min. A precision impedance analyzer (4294A, Agilent Technologies, Santa Clara, CA, USA) was used to analyze the temperature-dependent impedance spectra. The E_B measurement was performed at RT by using a voltage-withstand test device (BDJC-50KV, Beiguangjingyi Instrument Equipment Co. Ltd., Beijing, China). The temperature dependent *P-E* hysteresis loops were measured using a ferroelectric test system (Precision multiferroelectric; Radiant Technologies Inc, Albuquerque, New Mexico) connected with a high-temperature probing stage (HFS600E-PB2, Linkam Scientific Instruments, Tadworth, UK). The energy release properties of ceramic capacitors were investigated by a specially designed and highspeed capacitor discharge circuit. For pulsed charge-discharge test, the sample size is 0.2 mm (thickness) × 4.9 mm^2 (electrode area).

3. Results and discussion

Fig. 1 show the grain morphology of (0.94-*x*)NN-0.06BZ-*x*CZ ceramics sintered at their optimum temperatures. It can be seen that all the

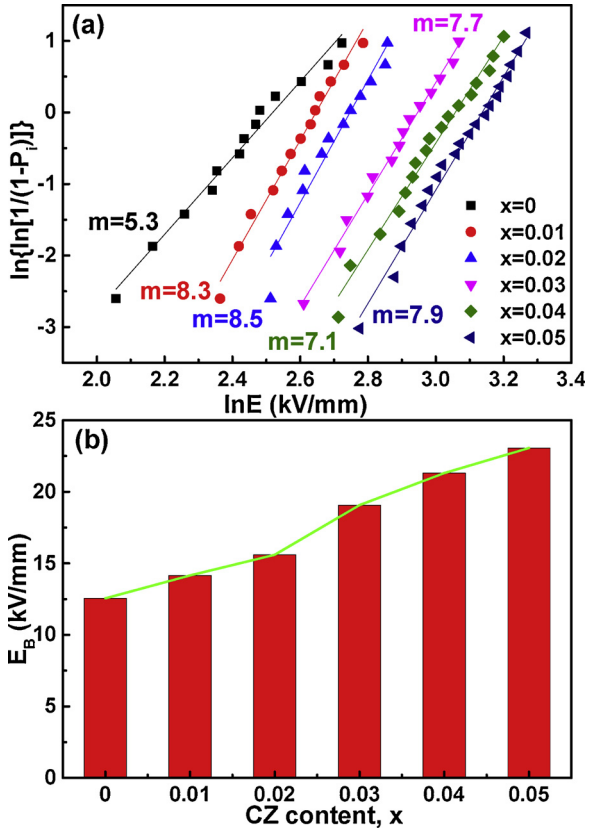

Fig. 3. (a) Weibull distributions and fitting lines of the E_B, and (b) the determined E_B as a function of CZ content.

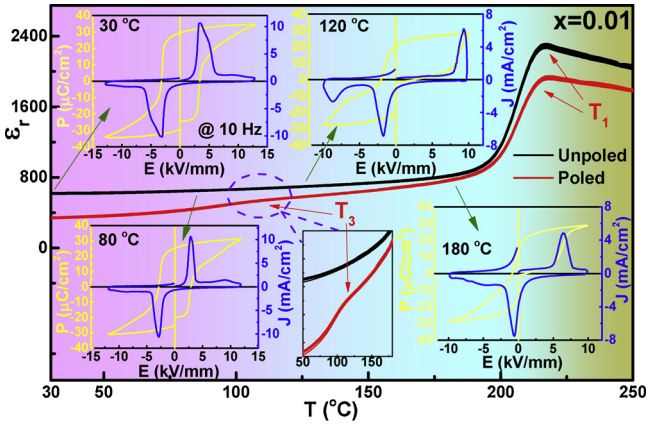

Fig. 5. Temperature dependent dielectric permittivity for unpoled and poled $x = 0.01$ ceramics; the insets show the *P-E* loops and the corresponding *J-E* curves measured at various temperatures.

studied samples were well sintered with a relative density of > 97% as proved by the Archimedes method. With the substitution of CZ for NN, the grain size of the sintered ceramic was found to decrease from ~3 μm at $x = 0$ to ~2 μm at $x = 0.04$ probably because of slightly decreased sintering temperature from the lattice activation. The E_B value was reported to have an exponential decay relationship with grain size (d), i.e., $E_B \propto (d)^{-a}$ because of the high resistivity of grain boundary based on the formation of the depletion space charge layers at the grain boundary [4].

The impedance (Z^*) is commonly used to clarify the conduction mechanism, and especially the relaxor behavior induced by defects. Fig. 2a shows the Z'-Z'' curves for several samples measured at 550 °C in the frequency range of 20 Hz-1 MHz, where Z' and Z'' are the real and

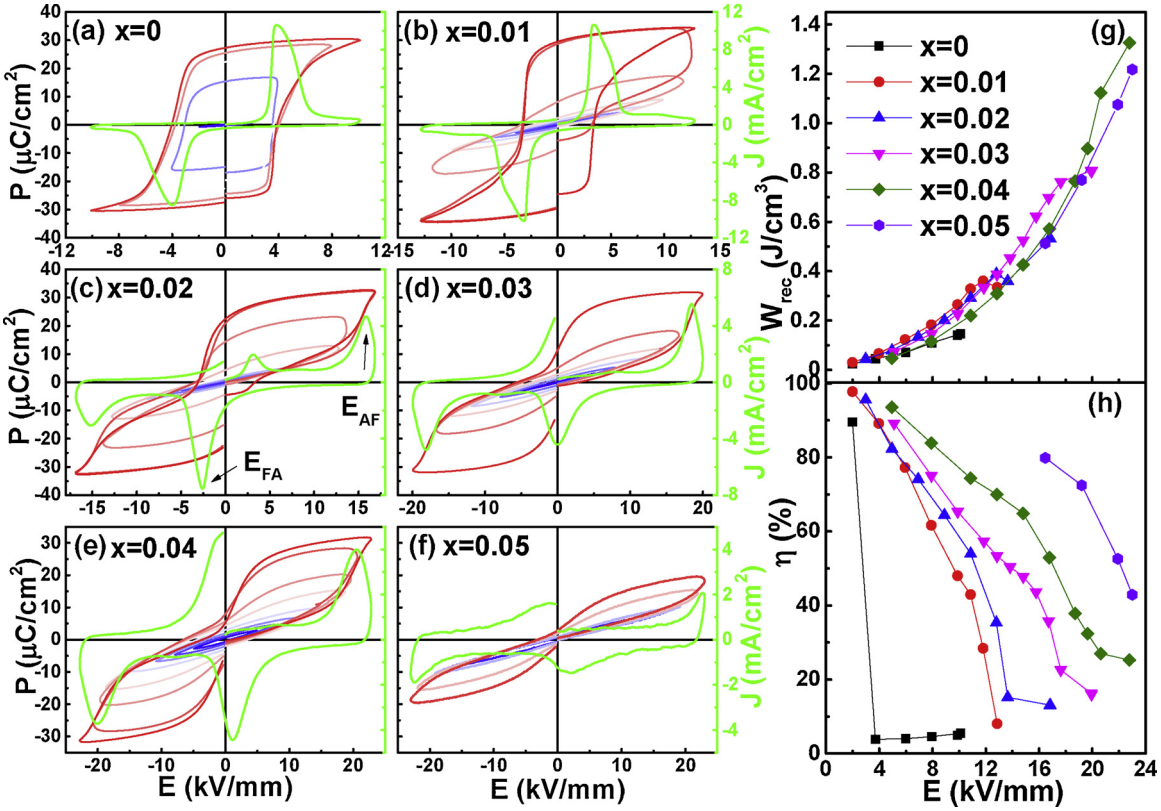

Fig. 4. (a)-(f) RT *P-E* loops measured under different electric fields and corresponding *J-E* curves under the maximum test electric field for (0.94-x)NN-0.06BZ-xCZ ceramics, and (g) W_{rec} and (h) η values of (0.94-x)NN-0.06BZ-xCZ ceramics varying with the magnitude of the applied electric field.

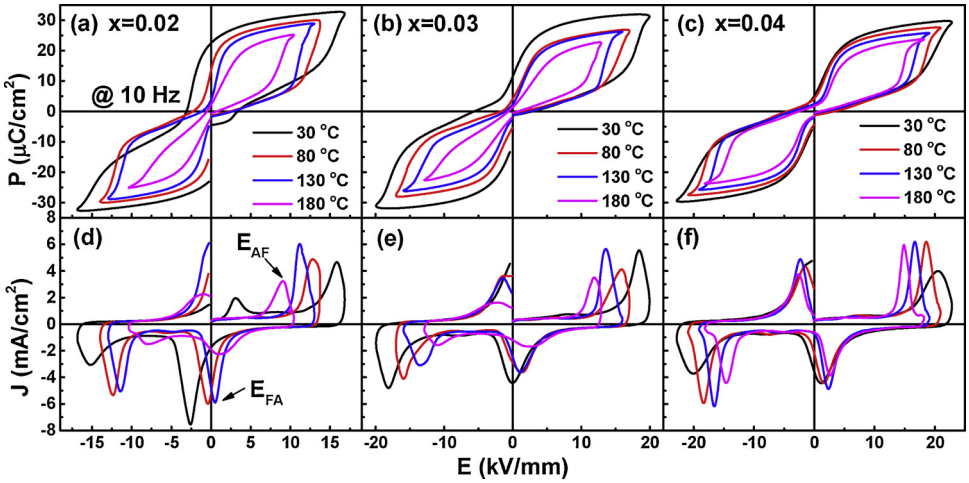

Fig. 6. Temperature dependent (a)-(c) *P-E* loops and (d)-(f) the corresponding *J-E* curves for a few (0.94-*x*)NN-0.06BZ-*x*CZ ceramics.

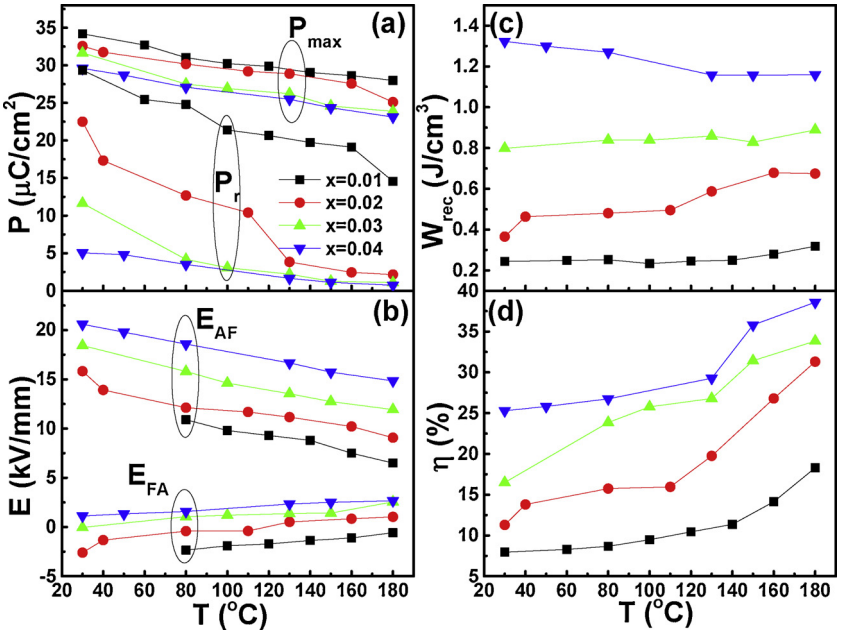

Fig. 7. Temperature dependence of (a) *Pmax* and P_r, (b) E_{AF} and E_{FA}, (c) W_{rec} and (d) η values for (0.94-*x*)NN-0.06BZ-*x*CZ ceramics.

imaginary parts of impedance, respectively. All the studied curves are a nearly single Debye semicircle arc. According to the fitting results, there is still a small contribution from grain boundary even though the conduction mechanism is mainly determined by grains. Furthermore, with the addition of CZ, the impedance increases monotonously in the studied composition range. This may be ascribed to the restriction of forming point defects owing to reduced volatilization of sodium as sintering temperature decreases with increasing CZ content. Fig. 2b shows the *Z"/Z"max* as a function of frequency for the $x = 0.04$ ceramic in the temperature of 450–600 °C. Only one peak can be observed, which shifts towards higher frequency with increasing temperature. This suggests that temperature dependent relaxation behavior is mainly induced by the defects or vacancies in the $x = 0.04$ ceramic. The activation energy (E_a), which is associated with the potential-energy barrier, can be estimated by the Arrhenius law [26]:

$$\sigma = \sigma_0 exp(E_a/kT) \quad (1)$$

where σ is the bulk conductivity, σ_0 is the pre-exponent constant and k is the Boltzmann constant. E_a can be calculated from the slope of $ln\sigma$-$1000/T$ plots and is in the range of 1.48–1.57 eV for different samples, as shown in Fig. 2c, meaning a main conduction mechanism from oxygen vacancies. The increased E_a value with increasing CZ content is also believed to be in favor of enhancing E_B, because the larger E_a may be attributed to more difficult long-range migration of oxygen vacancies, namely oxygen vacancies are steadier.

The Weibull distribution function is usually used for the E_B analysis due to the statistical nature of failure. [27] The values of E_B of (0.94-*x*) NN-0.06BZ-*x*CZ ceramics can be evaluated by using the following Weibull distribution functions:

$$X_i = ln(E_i) \quad (2)$$

$$Y_i = \ln\{\ln[1/(1-P_i)]\} \quad (3)$$

$$P_i = i/(n+1) \quad (4)$$

where n is the total number of the samples, E_i is the breakdown electric field for the ith specimen arranging in the ascending order, and P_i the probability of dielectric breakdown. X_i and Y_i should have a linear relationship and the slope is the Weibull modulus m. As shown in Fig. 3a, all the data points fit well with the Weibull distribution. The shape parameters m with values more than five were obtained for all the

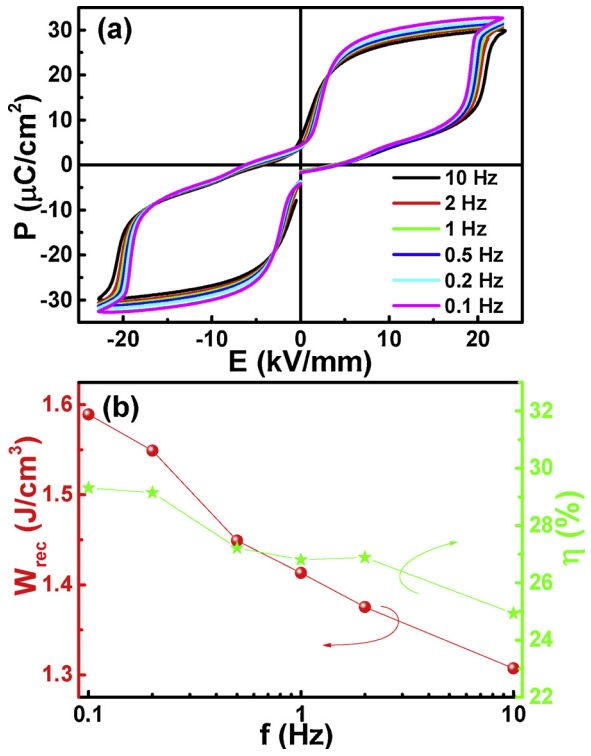

Fig. 8. Frequency dependent (a) *P-E* loops and (b) W_{rec} and η values for the $x = 0.04$ ceramics.

studied (0.94-*x*)NN-0.06BZ-*x*CZ ceramics, demonstrating high reliability of the Weibull analysis. The Weibull moduli E_B values were then determined through linear regression of the *ln(-ln(1-P$_i$))–lnE relation*, as indicated in Fig. 3b. The average E_B was found to increase monotonously with increasing CZ content in the studied composition range, with values on the order of 12 and 23 kV/mm for $x = 0$ and $x = 0.05$ ceramics, respectively.

The *P-E* loops measured under different electric fields as well as the corresponding polarization current density versus electric field (*J-E*) curves obtained under each maximum test electric field are shown in Fig. 4a–f for (0.94-*x*)NN-0.06BZ-*x*CZ ceramics. Square *P-E* loops conforming to the feature of a normal FE can be obtained in the $x = 0$ ceramic, indicating an irreversible AFE-FE phase transition. The sharp current peak on the corresponding *J-E* loop should be thus related to the fast domain switching around the coercive field. With the substitution of CZ for NN, a reproducible double-like *P-E* loop can be observed in the composition range of $0.01 < x \leq 0.05$, suggesting a stable antiferroelectricity although the AFE phase in these samples before and after poling is not completely the same in the crystal symmetry (AFE_O *Pbma*, AFE monoclinic *P2$_1$*) [25]. Moreover, the critical electric field values for the AFE-FE (E_{AF}) and FE-AFE (E_{FA}) phase transition, which were obtained according to the position of the polarization current peaks on *J-E* curves, increase with increasing CZ content. A large P_r value of over 10 μC/cm^2 was obtained at RT for compositions with $0.01 < x < 0.03$, even though reproducible double *P-E* loops can be generated in the $x = 0.02$ ceramic. This should be ascribed to the time hysteresis effect of the back switching from field induced FE phase to the AFE phase, corresponding to a negative E_{FA} value in the $x = 0.02$ ceramic at RT. P_r drops significantly at $x = 0.03$, suggesting a possible enhancement of energy-storage properties. Based on *P-E* hysteresis loops, the energy storage properties of (0.94-*x*)NN-0.06BZ-*x*CZ ceramics under different electric fields are shown in Fig. 4g and h. With increasing electric field, W_{rec} increases, while η decreases drastically especially as the electric field is close to the E_{AF} owing to the hysteresis between forward and backward switching from the AFE phase to the FE phase during charging and discharging processes, respectively. Even though E_B increases with increasing CZ content, W_{rec} increases first, then reaches its maximum value of ~1.32 J/cm^3 at $x = 0.04$, and finally decreases with further increasing *x*. The enhanced energy-storage properties at $x = 0.04$ should be ascribed to both reversible AFE-FE phase transition and improved dielectric breakdown strength.

Fig. 5 shows the temperature dependent permittivity values of both unpoled and poled samples with $x = 0.01$. An AFE phase can be identified for the virgin sample of $x = 0.01$ in the temperature range between RT and T_1 (the temperature for AFE P to AFE R phase transition). [25,28] After poling at RT, an FE phase can be achieved, as confirmed by a square *P-E* loop in the inset of Fig. 5. The electric field induced FE

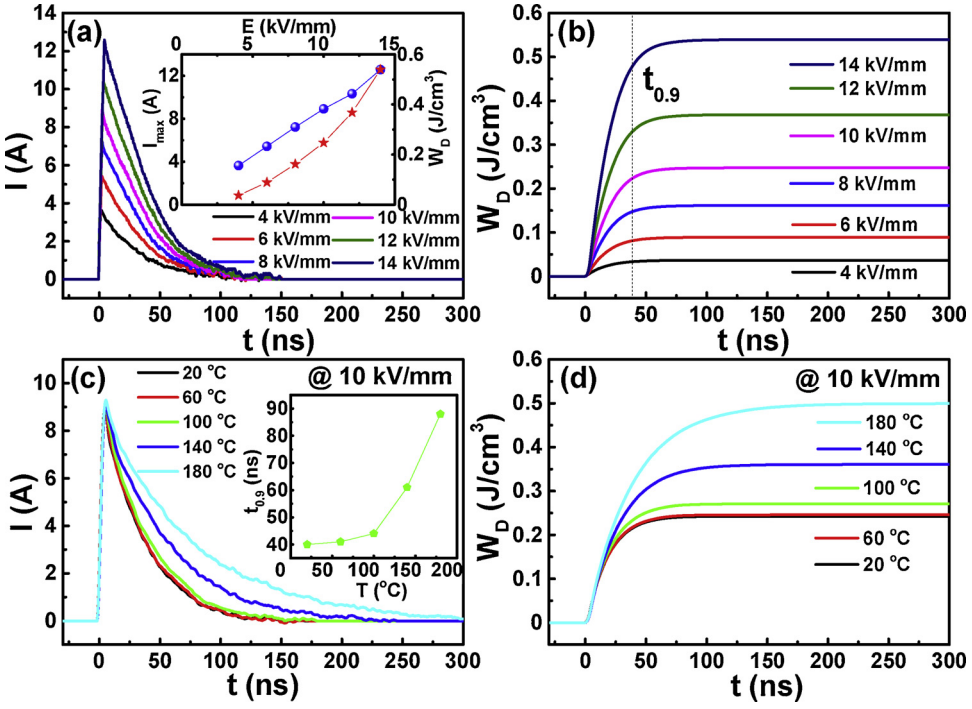

Fig. 9. (a) RT pulsed overdamped discharging current curves of the $x = 0.04$ ceramic at a fixed load resistance of 200 Ω under various electric fields; (b) W_D as a function of time for the $x = 0.04$ ceramic under various electric fields; (c) The temperature dependence of the pulsed overdamped discharging current curves of the $x = 0.04$ ceramic under 10 kV/mm; (d) W_D as a function of time at different temperatures. The inset of (a) is the variation of *Imax* and W_D as a function of the electric field. The inset of (c) is the variation of $t_{0.9}$ as a function of temperature.

phase would turn back to an AFE phase approximately at T_3~100 °C on heating, causing an obvious dielectric anomaly as shown by a locally magnified image in Fig. 5. Double hysteresis *P-E* loops as well as double current peaks on *J-E* curves can be detected only above T_3 (for example at 120 °C and 180 °C), indicating a stable antiferroelectricity. In addition, it is obvious that E_{AF} increases but E_{FA} decreases upon heating.

For the compositions with $x > 0.01$ with stable antiferroelectricity, typical double *P-E* loops accompanying with double current peaks can be observed in the temperature range from RT to 180 °C, as shown in Fig. 6. According to *P-E* loops measured at different temperatures (Fig. 6), *Pmax*, P_r, E_{AF}, E_{FA}, W_{rec} and η were plotted as a function temperature, as shown in Fig. 7. The value of *Pmax* decreases gradually with increasing temperature for all compositions. Accompanying the increase of E_{FA}, P_r decreases monotonously with increasing temperature, especially a drastic drop of P_r can be found when E_{FA} changes from negative to positive fields. As known, the discharge process is more important for the available energy storage density. Therefore, the increase in E_{FA} with increasing temperature should be in favor of the discharge energy storage behavior. Differently, the decrease in *Pmax* is not beneficial for the energy storage density, particularly for the $x = 0.04$ ceramic owing to its more stable antiferroelectricity. As a result, η increases all the time on heating for the studied composition, W_{rec} increases slightly for $0.01 \leq x \leq 0.03$ compositions but decreases slightly for the $x = 0.04$ ceramic. A large W_{rec} of > 1.16 J/cm^3 was achieved in the $x = 0.04$ ceramic in the temperature range from RT to 180 °C.

The P-E loops measured under different frequencies for the $x = 0.04$ ceramic is shown in Fig. 8a. With increasing the measuring frequency, the AFE-FE phase transition and the domain wall motion lag and then their contribution to the polarization level drops, leading to a reduction of *Pmax*. At the same time, the polarization hysteresis increases during the period of applying electric field, causing a decrease of E_{FA} but an increase of E_{AF}. As a consequence, both W_{rec} and η decreases slightly with increasing the measuring frequency, as shown in Fig. 8b. A large energy storage density of W_{rec} ~ 1.59 J/cm^3 together with a relatively low η of ~30% was obtained at 0.1 Hz in the $x = 0.04$ ceramic at RT. Therefore, it is essential in future to largely reduce the hysteresis of the AFE-FE phase transition in order to enable the NN-based AFE ceramics to be efficiently used for high-energy storage capacitor applications.

In order to evaluate the actual charging-discharging performance, the pulsed charging-discharging speed of the $x = 0.04$ ceramic was measured. Overdamped pulsed discharge electric current-time (*I–t*) curves measured at different electric fields and different temperatures are shown in Fig. 9. The discharge energy density (W_D) of the $x = 0.04$ ceramic can be calculated as:

$$W_D = R \int I(t)^2 dt / V \quad (5)$$

where R and V are total load resistor (200 Ω) and the sample volume, respectively. With increasing electric field from 4 kV/mm to 14 kV/mm, the current peak (*Imax*) and W_D values increase from 3.64 A and 0.037 J/cm^3 to 12.58 A and 0.54 J/cm^3, respectively, as shown in Fig. 9a and b. According to the W_D-*t* curves measured under different electric fields in Fig. 9b, the $x = 0.04$ ceramic shows a fast discharging speed with a short discharge time ($t_{0.9}$) ~40 ns, which describes the discharge time corresponding to reaching 90% saturated W_D value. When an external electric field of much lower than E_{AF} is applied on AFE ceramics, a nearly linear and hysteresis-free polarization response merely from the ionic displacement can be achieved (see Fig. 4). Therefore, after removal of external electric field, the stored energy during charging could be released within a short time, accompanying the fast decrease of polarization. It can be seen that the discharge current rapidly reaches the peak value in a remarkably short time at different temperatures under 10 kV/mm, as shown in Fig. 9c. Moreover, there is no evident change in *Imax* from 20 to 180 °C. However, a gradual increase of $t_{0.9}$ can be achieved on heating, as shown in Fig. 9d and the inset of Fig. 9c. This should be related to a gradual increase of the contribution of AFE domain reorientation and even AFE-FE phase transition owing to a slight decrease of E_{AF} on heating. On the one hand, the time effect of the back-switching of AFE domains and AFE-FE phase transition would cause an obviously enhanced polarization hysteresis, inducing the decline of the discharging speed. On the other hand, both charge and discharge energy density increase on heating owing to the increased contribution of AFE domain switching and AFE-FE phase transition. As a result, an increase in W_D from 0.24 J/cm^3 to 0.50 J/cm^3 is obtained when temperature increases from 20 °C to 180 °C.

4. Conclusions

A series of (0.94-*x*)NN-0.06BZ-*x*CZ lead-free ceramics were successfully fabricated via a conventional solid-state reaction method. Obviously enhanced stability of the antiferroelectricity was realized through the substitution of CZ for NN. Repeatable double P-E loops corresponding to reversible AFE-FE phase transition were achieved in compositions of $0.05 \geq x < 0.01$, resulting in a drastic enhancement of the energy storage properties. As a result, a high W_{rec} ~1.59 J/cm^3 (0.1 Hz) and a relatively η of ~30% as well as an ultra-fast discharge rate $t_{0.9}$ ~ 40 ns were achieved simultaneously at RT in the $x = 0.04$ ceramic. Moreover, a high W_{rec} of > 1.16 J/cm^3 can be generated from RT to 180 °C in the $x = 0.04$ ceramic. These results demonstrate that the (0.94-*x*) NN-0.06BZ-*x*CZ AFE_O P-phase ceramics can be considered as potential candidate lead-free materials for high-energy storage ceramic capacitors. The application potentials would be largely increased if the hysteresis of the AFE-FE phase transition can be effectively reduced by the compositional modification.

Acknowledgements

This work was financially supported by the National Natural Science Foundation of China (Grant No. 51472069) and the China Postdoctoral Science Foundation (Grant No. 2018M642998).

References

[1] B.J. Chu, X. Zhou, K.L. Ren, B. Neese, M.R. Lin, Q. Wang, F. Bauer, Q.M. Zhang, A dielectric polymer with high electric energy density and fast discharge speed, Science 313 (2006) 334–336.
[2] Z.H. Yao, Z. Song, H. Hao, Z.Y. Yu, M.H. Cao, S.J. Zhang, M.T. Lanagan, H.X. Liu, Homogeneous/inhomogeneous-structured dielectrics and their energy-storage performances, Adv. Mater. 29 (2017) 1601727.
[3] H.S. Wang, Y.C. Liu, T.Q. Yang, S.J. Zhang, Ultrahigh energy-storage density in antiferroelectric ceramics with field-induced multiphase transitions, Adv. Funct. Mater. (2018) 1807321.
[4] L.T. Yang, X. Kong, F. Li, H.H, Z.X. Cheng, H.X. Liu, J.F. Li, S.J. Zhang, Perovskite lead-free dielectrics for energy storage applications, Prog. Mater. Sci. 102 (2019) 72–108.
[5] X.H. Hao, A review on the dielectric materials for high energy-storage application, J. Adv. Dielect. 3 (2013) 1330001.
[6] A. Chauhan, S. Patel, R. Vaish, C.R. Bowen, Anti-ferroelectric ceramics for high energy density capacitors, Materials 8 (2015) 8009–8031.
[7] L. Zhang, S.L. Jiang, B.Y. Fan, G.Z. Zhang, Enhanced energy storage performance in $(Pb_{0.858}Ba_{0.1}La_{0.02}Y_{0.008})(Zr_{0.65}Sn_{0.3}Ti_{0.05})O_3$-$(Pb_{0.97}La_{0.02})(Zr_{0.9}Sn_{0.05}Ti_{0.05})O_3$ anti-ferroelectric composite ceramics by spark plasma sintering, J. Alloy Compd. 622 (2015) 162–165.
[8] Y. Dan, H.J. Xu, K.L. Zou, Q.F. Zhang, Y.M. Lu, G. Chang, H.T. Huang, Y.B. He, Energy storage characteristics of $(Pb,La)(Zr,Sn,Ti)O_3$ antiferroelectric ceramics with high Sn content, Appl. Phys. Lett. 113 (2018) 063902.
[9] Z. Liu, X.F. Chen, W. Peng, C.H. Xu, X.L. Dong, F. Cao, G.S. Wang, Temperature-dependent stability of energy storage properties of $Pb_{0.97}La_{0.02}(Zr_{0.58}Sn_{0.335}Ti_{0.085})O_3$ antiferroelectric ceramics for pulse power capacitors, Appl. Phys. Lett. 106 (2015) 262901.
[10] Y. Tian, L. Jin, H.F. Zhang, Z. Xu, X.Y. Wei, E.D. Politova, S.Y. Stefanovich, N.V. Tarakina, I. Abrahams, H.X. Yan, High energy density in silver niobate ceramics, J. Mater. Chem. A 4 (2016) 17279–17287.
[11] L. Zhao, Q. Liu, J. Gao, S.J. Zhang, J.F. Li, Lead-free antiferroelectric silver niobate tantalate with high energy storage performance, Adv. Mater. 29 (2017) 1701824.
[12] J.L. Li, F. Li, Z. Xu, S.J. Zhang, Multilayer lead-free ceramic capacitors with ultra-high energy density and efficiency, Adv. Mater. 30 (2018) 1802155.
[13] H. Borkar, V.N. Singh, B.P. Singh, M. Tomar, V. Gupta, A. Kumar, Room temperature lead-free relaxor-antiferroelectric electroceramics for energy storage

applications, RSC Adv. 4 (2014) 22840–22847.
[14] Z.Y. Liu, J.S. Lu, Y.Q. Mao, P.R. Ren, H.Q. Fan, Energy storage properties of $NaNbO_3$-$CaZrO_3$ ceramics with coexistence of ferroelectric and antiferroelectric phases, J. Eur. Ceram. Soc. 38 (2018) 4939–4945.
[15] B.C. Luo, H.J. Dong, D.Y. Wang, K.X. Jin, Large recoverable energy density with excellent thermal stability in Mn-modified $NaNbO_3$-$CaZrO_3$ lead-free thin films, J. Am. Ceram. Soc. 101 (2018) 3460–3467.
[16] S.K. Mishra, N. Choudhury, S.L. Chaplot, P.S.R. Krishna, R. Mittal, Competing antiferroelectric and ferroelectric interactions in $NaNbO_3$: neutron diffraction and theoretical studies, Phys. Rev. B 76 (2007) 024110.
[17] S.K. Mishra, R. Mittal, V.Y. Pomjakushin, S.L. Chaplot, Phase stability and structural temperature dependence in sodium niobate: a high-resolution powder neutron diffraction study, Phys. Rev. B 83 (2011) 134105.
[18] G.O. Jones, P.A. Thomas, Investigation of the structure and phase transitions in the novel A-site substituted distorted perovskite compound $Na_{0.5}Bi_{0.5}TiO_3$, Acta Cryst. B 58 (2002) 168–178.
[19] D. Fu, M. Endo, H. Taniguchi, T. Taniyama, M. Itoh, $AgNbO_3$: a lead-free material with large polarization and electromechanical response, Appl. Phys. Lett. 90 (2007) 252907.
[20] Y.I. Yuzyuk, P. Simon, E. Gagarina, L. Hennet, D. Thiaudière, V.I. Torgashev, S.I. Raevskaya, I.P. Raevskii, L.A. Reznitchenko, J.L. Sauvajol, Modulated phases in $NaNbO_3$: raman scattering, synchrotron x-ray diffraction, and dielectric investigations, J. Phys. Condens. Matter 17 (2005) 4977–4990.
[21] H.Z. Guo, H. Shimizu, C.A. Randall, Direct evidence of an incommensurate phase in $NaNbO_3$ and its implication in $NaNbO_3$-based lead-free antiferroelectrics, Appl. Phys. Lett. 107 (2015) 112904.
[22] H. Shimizu, K. Kobayashi, Y. Mizuno, C.A. Randall, Advantages of low partial pressure of oxygen processing of alkali niobate: $NaNbO_3$, J. Am. Ceram. Soc. 97 (2014) 1791–1796.
[23] Y.H. Xu, W. Hong, Y.J. Feng, X.L. Tan, Antiferroelectricity induced by electric field in $NaNbO_3$-based lead-free ceramics, Appl. Phys. Lett. 104 (2014) 052903.
[24] H. Shimizu, H.Z. Guo, S.E. Reyes-Lillo, Y. Mizuno, K.M. Rabe, C.A. Randall, Lead-free antiferroelectric: $xCaZrO_3$-(1-x)$NaNbO_3$ system ($0 \leq x \leq 0.10$), Dalton Trans. 44 (2015) 10763–10772.
[25] R.Z. Zuo, J. Fu, H. Qi, Stable antiferroelectricity with incompletely reversible phase transition and low volume-strain contribution in $BaZrO_3$ and $CaZrO_3$ substituted $NaNbO_3$ ceramics, Acta Mater. 161 (2018) 352–359.
[26] K.J. Laidler, The development of the Arrhenius equation, J. Chem. Educ. 61 (1984) 494–498.
[27] J.J. Huang, Y. Zhang, T. Ma, H.T. Li, L.W. Zhang, Correlation between dielectric breakdown strength and interface polarization in barium strontium titanate glass ceramics, Appl. Phys. Lett. 96 (2010) 042902.
[28] M.X. Dou, J. Fu, R.Z. Zuo, Electric field induced phase transition and accompanying giant poling strain in lead-free $NaNbO_3$-$BaZrO_3$ ceramics, J. Eur. Ceram. Soc. 38 (2018) 3104–3110.